

Article

Numerical Investigation on Detonation Initiation and Propagation with a Symmetric-Jet in Supersonic Combustible Gas

Jian Dai *  and Linyuan Peng

Research Institute of Aerospace Technology, Central South University, Changsha 410083, China

* Correspondence: daijian@csu.edu.cn

Abstract: In this study, supersonic gaseous detonation initiation and propagation by single- and symmetric-jets are compared, and the effects of symmetric-jets of different intensities on the detonation are further investigated to obtain a more comprehensive understanding of the initiation mechanism of hot jet in supersonic mixtures. The two-dimensional reactive Navier–Stokes equations, together with a one-step Arrhenius chemistry model, are adopted to analyze the flow field structure. The results show that the bow shocks induced by symmetric-jets interacting with each other will achieve local detonation combustion. Influenced by the unstable shear layer behind the triple point, a large-scale vortex shedding is formed in the flow field, thus promoting the consumption of the unburned region. By comparing with the single-jet, it is found that the dual-jet initiation method can shorten the distance to complete initiation, but has little effect on the detonation overdrive degree. In addition, a study of the impact of jet size parameters on the symmetric-jet initiation further revealed that there is a critical value, above which the ignition decreases rapidly which is a significant advantage over single-jet. However, below this threshold, detonation initiation will rely on the energy generated by the collision of Mach stems formed at the walls, resulting in a slower ignition rate compared to a single-jet. Therefore, the use of the appropriate jet strength when using a symmetric-jet will result in a more desirable ignition velocity and a shorter distance to achieve detonation.

Keywords: detonation wave; hot jet initiation; symmetric-jet; supersonic combustible mixture



Citation: Dai, J.; Peng, L. Numerical Investigation on Detonation Initiation and Propagation with a Symmetric-Jet in Supersonic Combustible Gas. *Aerospace* **2022**, *9*, 501. <https://doi.org/10.3390/aerospace9090501>

Academic Editor: Fabrizio Ponti

Received: 26 July 2022

Accepted: 7 September 2022

Published: 8 September 2022

Publisher's Note: MDPI stays neutral with regard to jurisdictional claims in published maps and institutional affiliations.



Copyright: © 2022 by the authors. Licensee MDPI, Basel, Switzerland. This article is an open access article distributed under the terms and conditions of the Creative Commons Attribution (CC BY) license (<https://creativecommons.org/licenses/by/4.0/>).

1. Introduction

Scramjet exhibits excellent operating performance under a high Mach number ($Ma \geq 5.0$) and has become the mainstream power structure of hypersonic aircraft [1,2]. The existing scramjet usually uses the isobaric mode to organize combustion, which limits the improvement of propulsion performance [3]. To meet the higher requirements for propulsion performance of future hypersonic vehicles, a concept of scramjet based on detonation combustion was proposed [4]. The new type of detonation combustion power device is gradually becoming a potential power method for improving the thrust performance of hypersonic vehicles owing to its higher thermal cycle efficiency and heat release rate [5–7]. It should be noted that the reliable ignition and stable propagation of detonation waves in a supersonic flow field are the core problems that need to be solved urgently [8]. Among them, hot jet initiation is a promising method for detonation initiation [9] as it bypasses the flame acceleration process during deflagration to detonation transition (DDT) [10,11], allowing the propellant to be detonated rapidly. Ishii et al. [12] investigated the detonation initiation using hot jets in combustible mixtures with Mach numbers of 0.9 and 1.2 via experimental observations; they discovered that changing incoming flow velocity would lead to different detonation wave velocities. Han et al. [13] conducted an experimental study regarding detonation initiation caused by a hot jet in a supersonic premixed gas; they discovered that the detonation was induced by a shock wave induced by the hot jet on a wall. Chen et al. [14] used the Adaptive Mesh Refinement Object-oriented C++ (AMROC) [15,16] program to simulate the high-resolution hot jet initiation process and

suggested that a bow shock wave was reflected on the wall and formed a Mach reflection, followed by a local detonation behind the Mach stem. Subsequently, the triple points on the shock front collided, causing the entire flow field to detonate. These previous studies show that a hot jet can rapidly initiate detonation by inducing a shock wave that is reflected on the wall.

The above-mentioned studies have primarily focused on the single-jet initiation arrangement. Although considerable results have been obtained regarding the propagation of single-jet detonation in supersonic premixed gas, results obtained using the dual-jet initiation method are scarce. Cai et al. [17] used a three-dimensional numerical simulation to compare the effects of a single-jet and a collision double jet in a supersonic premixed gas tube on the formation of detonation waves, whereas the initiation propagation process of the dual jet has not been investigated comprehensively, and the performance difference between the two initiation methods remains unclear. In the existing dual-jet detonation studies, Peng et al. [18,19] used experimental observations and numerical simulations to investigate the DDT of a methane-oxygen mixed jet in a pulsed detonation engine (PDE) [20] combustion chamber under various double jet modes; the results show that the vortex caused by the dual jet can cause distortion and wrinkles on the flame front, increasing the turbulence intensity, as well as causing the dual jet mode to exhibit a higher DDT velocity than the single-jet mode. Under different jet parameter settings, a higher intensity jet will result in more compression waves, thereby accelerating the flame propagation speed. Wang et al. [21] observed the effect of the position of a dual jet on the detonation of a PDE and discovered that the distance between the first jet and the second jet was sensitive to the detonation process and the interaction of the shock wave. It was observed that in the PDE detonation chamber, the dual jet initiation method afforded a more significant advantage than the single-jet, whereas different jet arrangements significantly affected the detonation process. Unlike in static air, under the condition of supersonic flow, a hot jet is affected by high-speed flows after it enters the main flow, which is different from the initiation process in a PDE. If the collision dual jet initiation method is used in supersonic combustible gas, in addition to the appropriate jet parameters and injection time, then a smooth generation of detonation waves may be achieved using low ignition energy.

The main objective of this work is to investigate the interaction process between jets and their effect on the detonation characteristics in a supersonic combustible mixture with two (double) hot jets as the ignition source. In addition, the high-temperature and pressure combustion products generated by the jet hole will cause the disturbance of the combustion chamber while igniting the main detonation chamber, increasing the turbulence intensity. Therefore, in this work, we further explore the role of fine turbulent flow features after the detonation front, such as aerodynamic instability (including Richtmyer–Meshkov Instability [22] and Kelvin–Helmholtz Instability [23]) triggered by turbulent mixing on the consumption mechanism of the unburned mixture, which will directly or indirectly affect the structure and propagation mode of the detonation wave. The simulation results can provide a significant reference for the practical application of the scramjet based on detonation combustion. In the present work, an adaptive mesh refinement code AMROC has been used to perform high-resolution simulations of two-dimensional detonation, which dynamically refines the mesh according to the changes in flow field parameters at different moments. Mesh refinement is carried out in the region where the flow field parameters change sharply, and low mesh refinement or no refinement is carried out in the region where the flow field parameters change slowly. It can ensure the accuracy of the calculation and improve the efficiency of the calculation. This procedure has been validated in multiple-dimensional detonation simulations [24,25].

2. Computational Model

2.1. Computational Setup

A simplified schematic of the computational model is shown in Figure 1. In practical application, the engine is basically circular in cross section. The two-dimensional combus-

tion chamber model used in this paper is a cross-section of a three-dimensional circular tube combustion chamber, which can be considered as a rectangular straight channel. The hot jet hole set corresponds to the slot jet under three-dimensional conditions. The opposite side jets are symmetrically distributed. For the condition setting of impinging double hot jets, the critical aspect of the detonation initiation is the interaction of bow shock waves in the flow field. Thus, the sliding reflection boundary conditions are used for both the upper and lower walls. An inlet condition is set on the walls to simulate the hot jets, and a time variable is set to control the injection time of the hot jets. The right side boundary is designated as the inlet stream, specifying the static pressure, static temperature, Mach number, and component mass fraction. The left supersonic exit condition is set as the first-order extrapolation of all variables. In addition, the red box area is the observation area of our convection field structure, which is also the area shown in the figures provided in the subsequent numerical study. The red arrow represents the direction of the hot jet injection.

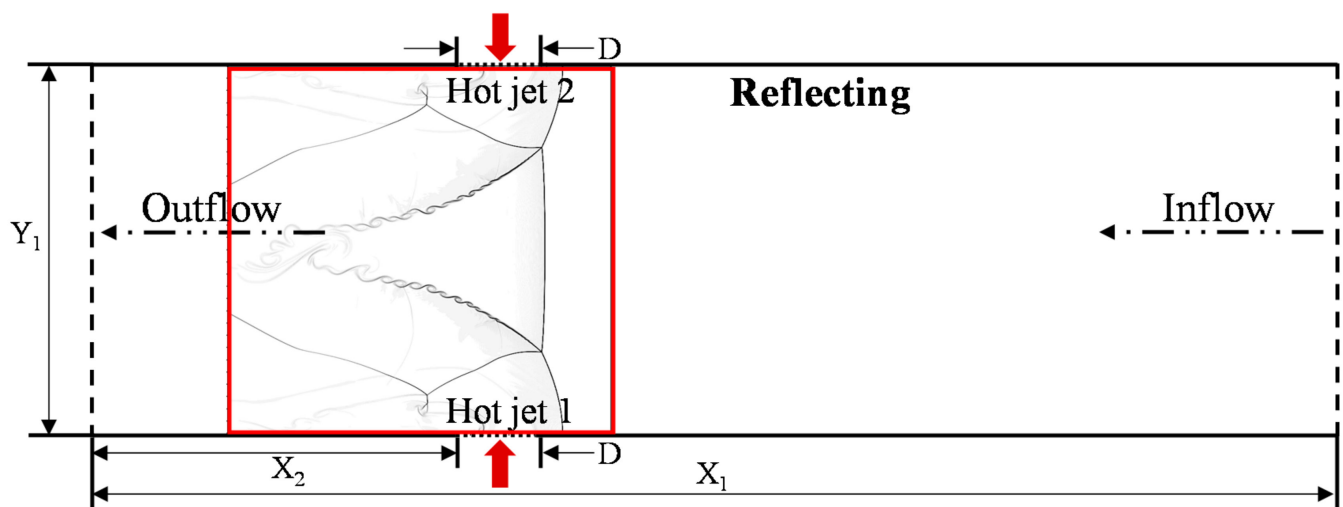


Figure 1. Schematic illustration of calculation model.

In this study, a supersonic hydrogen-oxygen mixture with a molar ratio of 2:1 is used. The initial pressure and temperature are set to 6.67 kPa and 300 K, respectively. The supersonic inlet velocity is set to the CJ detonation velocity (V_{CJ} 1587.84 m/s) for the above conditions. Self-sustaining CJ detonation in low-pressure hydrogen-oxygen mixtures is an ideal candidate for numerical simulations of detonation initiation in supersonic combustibles because it produces very regular detonation cell patterns [26]. The basic inlet parameters are listed in Table 1, and the cell size of the CJ detonation under this inflow condition is $\lambda = 25$ mm [27]. The length and width of the combustion chamber are $X_1 = 100$ mm and $Y_1 = 30$ mm, respectively. This means that a complete detonation cell can be observed in the Y direction, thus facilitating observation and analysis. The two hot jets have the same diameter, with jet width D. The distance between the hot jets and the outflow boundary is $X_2 = 40$ mm. The hot jet parameters are set to the equilibrium CJ state for the current incoming flow conditions. The equilibrium CJ state is calculated using the open-source chemical kinetics software Cantera [28], as shown in Table 2.

Table 1. Basic inflow parameters.

Parameters	Values	Unit
P_∞	6.67	kPa
T_∞	300	K
ρ_∞	0.077552	kg/m ³
V_∞	1587.84 (CJ detonation velocity)	m/s
Specific heat ratio of the mixed gas, γ	1.29499	-
Molecular quantity, W	0.029	kg/mol
Heat release per unit mass, q	54,000	J/mol
Activation energy, E_a	30,000	J/mol
Frequency factor, A	6×10^5	s ⁻¹
Molar gas constant of the chemical reaction, R	8.314	-

Table 2. Equilibrium CJ state of hot jet.

Parameters	Values	Unit
P_{CJ}	86.376	kPa
T_{CJ}	1943.8	K
ρ_{CJ}	0.155	kg/m ³
V_j	850 (speed of sound)	m/s
Total energy per unit mass, e	349,280	J/mol
Mass fraction of reactant, Y_1	0.0088	-
Mass fraction of product, Y_2	0.9912	-

2.2. Governing Equations and Numerical Methods

The interaction of the vortex formed by the dual jet in the static air flow field and the combustion front enhances the intensity of the turbulence, which contributes significantly to the detonation process [18]. To accurately simulate small-scale flow details such as turbulence and vortices, the two-dimensional Navier–Stokes equation is adopted as the governing equation [29].

Currently, the computational resources required to solve the Navier–Stokes equation using detailed chemical reaction methods are large. In this study, a one-step Arrhenius chemistry model is used to solve the Navier–Stokes equation [30]. Here the reaction model is selected and fitted to the detonation physical parameters of the H₂/O₂ combustible gas. The details of the chemical reaction model and the corresponding selection of thermodynamic parameters can also be found in studies by Ziegler [31]. Chen et al. [32] conducted numerical simulations of three-dimensional detonation waves with this reaction mechanism, and verified the reliability of the mechanism by comparing the numerical simulation results with the available experimental results. It should be noted that the weakness of this chemistry model is that it is unable to capture the chain-branching characteristics of the reactions and the corresponding crossover effects [33], and only the state parameters before and after the detonation wave are considered. However, it can visually reveal the physical nature of the detonation, which helps to qualitatively analyze the structure of the detonation and the effect of the jet parameters on the state of the detonation. Additionally, Arrhenius' law, which relates chemical reaction rates to temperature changes, is also widely used as the simplest model for the detonation simulation [34–36]. The two-species one-step reaction model is set using the ideal thermal cycle condition, as follows:

$$\gamma = \gamma_1 = \gamma_2, p = \rho RT, R = R_1 = R_2 \quad (1)$$

where γ is the Specific heat ratio of the mixed gas; R is the Molar gas constant of the chemical reaction; and the Subscripts 1 and 2 represent reactant and product, respectively.

The chemical reaction rate of the reactant and product is expressed by the Arrhenius formula, as follows:

$$\dot{w}_1 = -\dot{w}_2 = \rho Y_1 A \exp\left(-\frac{E_a}{RT}\right) \quad (2)$$

where \dot{w} is the chemical reaction rate; A is the pre-exponential factor; and E_a is the activation energy.

The temperature and pressure at the end of the Zel'dovich–von Neumann–Döring (ZND) reaction zone are calculated by fitting the physical parameters of a hydrogen–oxygen mixture with a stoichiometric ratio of 2:1 at an initial temperature of 300 K and a pressure of 6.67 kPa. The viscosity (μ) and conductivity (k) are obtained by the Sutherland mode [37], and mass diffusion (D) is obtained using a simplified formula inversely proportional to pressure, as follows:

$$\frac{\mu}{\mu_{ref}} = \left(\frac{T}{T_{ref}}\right)^{\frac{5}{2}}, \quad \frac{k}{k_{ref}} = \left(\frac{T}{T_{ref}}\right)^{\frac{5}{2}}, \quad (3)$$

$$\frac{D_1}{D_{1ref}} = \frac{p_{atm}}{p} \left(\frac{T}{T_{ref}}\right)^{\frac{5}{2}}, \quad \frac{D_2}{D_{2ref}} = \frac{p_{atm}}{p} \left(\frac{T}{T_{ref}}\right)^{\frac{5}{2}}. \quad (4)$$

where the transport parameters of the one-step reaction model are given as: $T_{ref} = 2500$ K, $\mu_{ref} = 1.07 \times 10^{-4}$ Pa·s, $k_{ref} = 0.148$ W/(m·K), $D_{1ref} = 5.5 \times 10^{-4}$ m²/s, and $D_{2ref} = 6.4 \times 10^{-4}$ m²/s.

The flux term is discretized using a hybrid sixth-order WENO-CD format with low dissipation characteristics and strong shock wave capture [38]. Meanwhile, the optimal third-order strong stability-preserving Runge–Kutta format is used for the chemical reaction source term [39], and the target CFL number is set to 0.98. For source-term integration, time splitting and the fourth-order-accurate semi-implicit stable generalized fourth-order Runge–Kutta method are used [40].

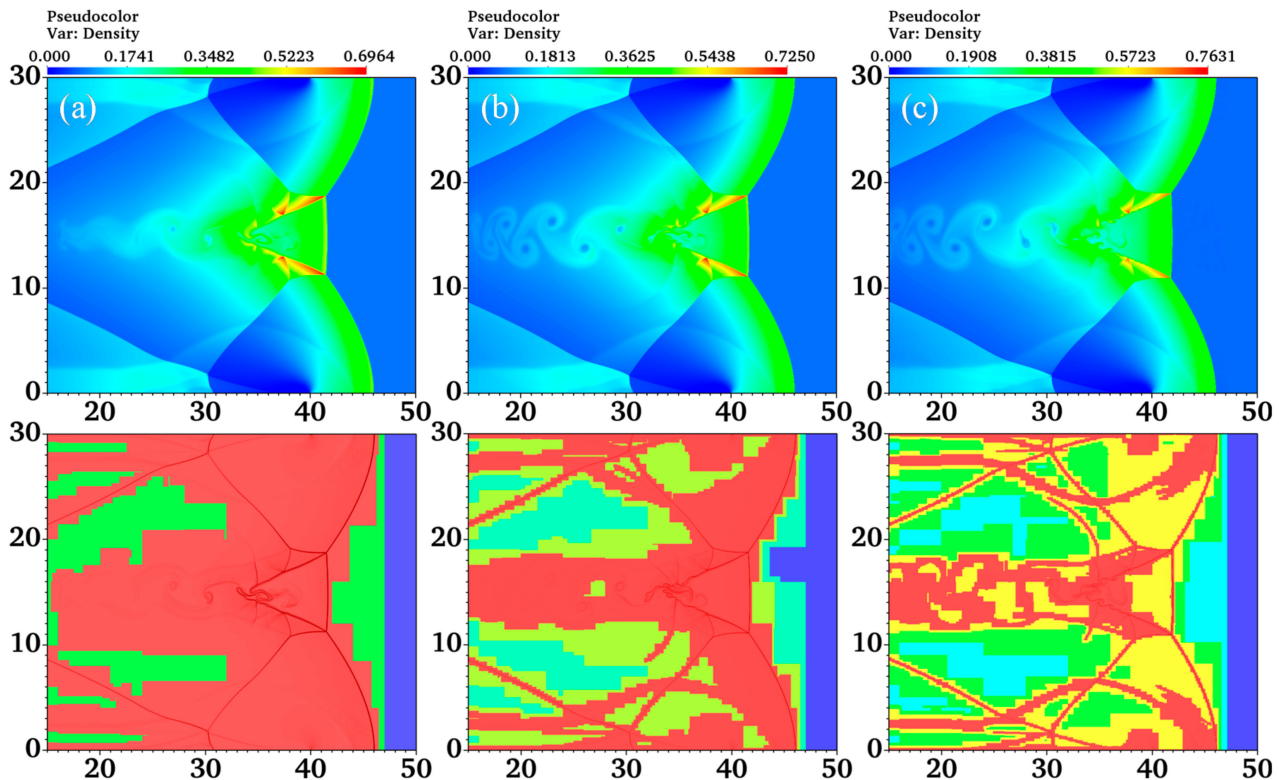
2.3. Mesh Refinement Verification

A suitable grid resolution is extremely important to achieve an accurate numerical simulation of the detonation. When the detonation wave propagates at 1000 m/s~2000 m/s, the distance between the leading shock wave and the combustion surface is only on the order of millimeters, which requires the use of a high-precision grid for accurate simulation and leads to an increase in the amount of numerical grid calculations.

To verify the adaptive densification effect of the numerical simulation procedure, three different adaptive mesh refinement implementations are built to verify the accuracy of the grid. The detailed grid parameters are listed in Table 3. The initial grid size used in this study is 800×240 , and the corresponding initial grid accuracy is 1.25×10^{-4} m. The length of the one-dimensional ZND reaction zone, $L_{hr} = 2.145$ mm, under the current conditions used in our study. Figure 2 shows a cloud plot of the refinement level for the three refinement calculation examples at $162.5 \mu\text{s}$. The red color indicates the region with the highest refinement level. As shown in the figure, all three refinement methods accurately capture the bow shock wave, Mach stem, and slip line in the flow field, and the regions with large variations of these parameters are at the highest refinement levels. Therefore, these three refinement methods meet the requirements of the numerical simulation. Combining the computational efficiency and computational accuracy, the highest grid resolution for the simulation is 137.28 Pts/Lhr (points per half-reaction length) using four levels of refinement in the numerical simulation. Deiterding's [41] study shows that a grid accuracy of 44.8 Pts/Lhr is sufficient to effectively identify the secondary triple point structure in a two-dimensional cellular lattice detonation simulation. Therefore, the grid resolution used in the current study can obtain reliable simulation results.

Table 3. Mesh refinement parameters.

	Three-Level	Four-Level	Five-Level
Refinement factors	(2, 2)	(2, 2, 2)	(2, 2, 2, 2)
Δ_{\min}	3.125×10^{-5} m	1.5625×10^{-5} m	7.8125×10^{-6} m
Resolution	68.64 Pts/Lhr	137.28 Pts/Lhr	274.56 Pts/Lhr

**Figure 2.** Three adaptive mesh refinement cases: (a) Three-level, (b) Four-level, and (c) Five-level. (Top row: contours of density at 162.5 μ s. Bottom row: refinement effects of three levels.)

Ziegler [31] found that the viscous scale is the smallest among the three diffusion scales (viscous shear layer, mass diffusion layer and thermal heat conduction layer), indicating that the resolution for the viscous scale determines the overall solution accuracy. The minimum grid accuracy of the four-level refinement used in this paper is 1.5625×10^{-5} m. The diffusive scale of viscosity in Figure 2b is estimated to be 7.54×10^{-5} m. This shows that at this grid resolution, about 5 cells can be placed in the viscous scale, so these diffusion scales can be fully resolved in this simulation. However, more details of the turbulent structures such as vortex stretching are not necessarily ready to distinguish, and thus a pseudo-direct numerical simulation is performed.

3. Results and Discussions

3.1. Analysis of the Detonation Induced by a Single-Jet

Figure 3 shows the initiation process of single-jet detonation of supersonic gas. The jet diameter is set to 8 mm to ensure that the single-jet and symmetric-jet inject the same amount of energy per unit time. As shown in Figure 3a, a hot jet injected at the local speed of sound enters the supersonic gas and blocks the incoming flow, thus inducing a bow shock wave in front of the jet. Under the continuous injection of the hot jet, the bow shock gradually develops outward and later collides with the upper wall surface. Figure 3b shows the reflected shock wave. Despite the further increase in density and pressure of the gas compressed by the reflected shock, at this time the reflected shock strength still cannot achieve detonation, only the formation of shock wave-induced combustion. With

the intensity of the reflected shock wave increasing, the regular reflection at the wall is transformed into a Mach reflection, and the Mach stem is developed at the original reflection point. In Figure 3c, Mach reflection is formed near the upper wall at this time. This is a sign indicating the formation of local detonation. Since the intensity of the jet-induced bow shock is greatest at the jet nozzle, the primary triple point is propagating down, as shown in Figure 3d. The flow field structure presented in the numerical simulation is generally consistent with the experimental observations of Cai et al. [42]. This is particularly true for the bow shock, wall reflection shock, and transverse wave. However, it should be noted that the sliding reflection boundary conditions are used for both the upper and lower walls in the calculations, and that the complex interactions of the boundary layer at the wall with the shock (such as the separation zone) in the experiment could not be represented in the numerical simulation results.

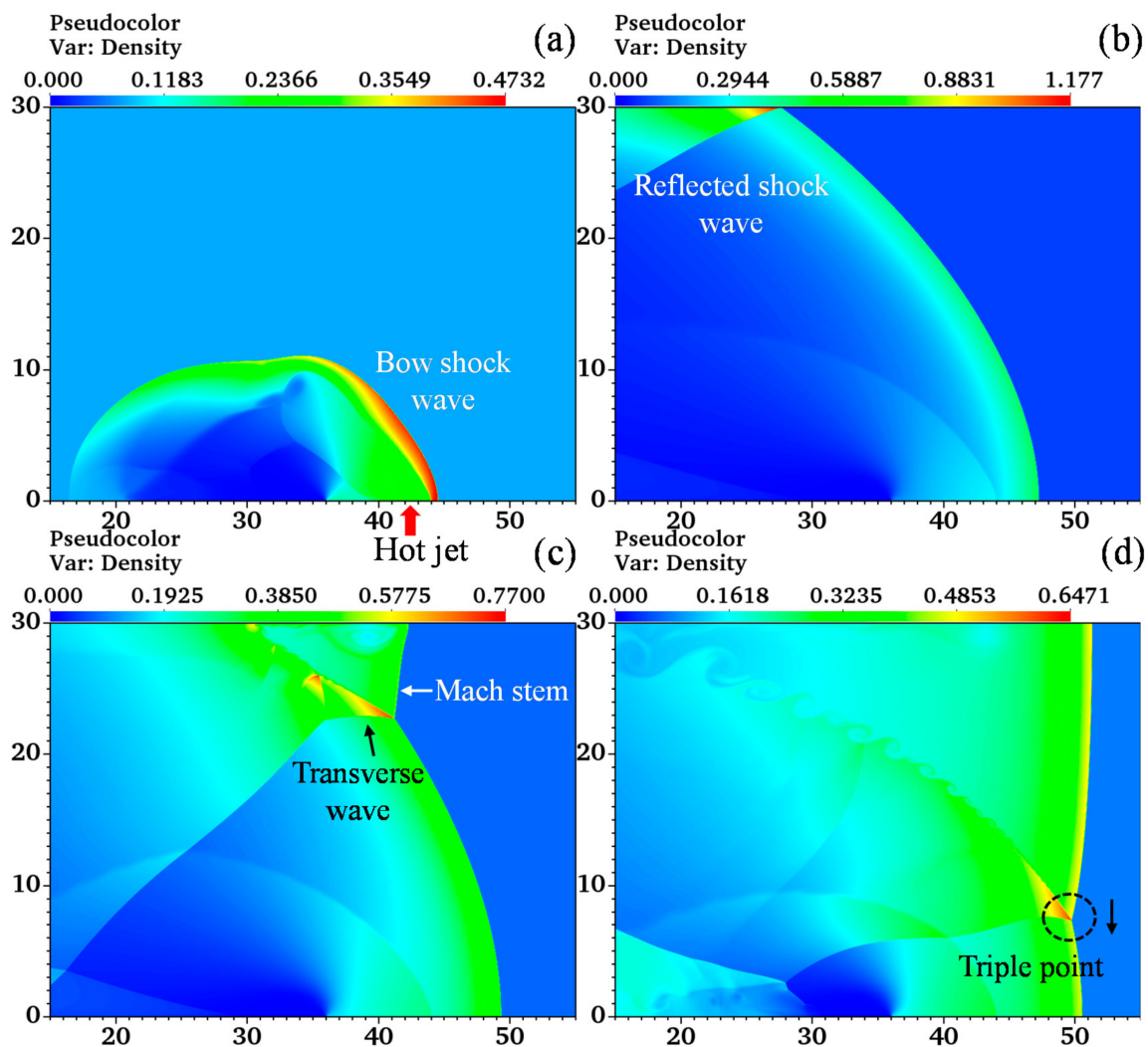


Figure 3. Density contours showing detonation initiation in straight channel, with continuous injection of a single-jet: (a) $t = 110 \mu\text{s}$; (b) $t = 130 \mu\text{s}$; (c) $t = 145 \mu\text{s}$; (d) $t = 170 \mu\text{s}$.

Figure 4 demonstrates the contour of reaction progress variable of the supersonic combustible mixture during the movement to the lower wall of the primary triple point T along with the bow shock, after the Mach stem is generated on the upper wall surface. As shown in Figure 4a, the Mach stem is closely coupled to the post-wave combustion products, indicating that localized detonation combustion has formed behind the Mach stem. Because of the relatively weak intensity of the bow shock, an unburned jet is formed below the slip line of the triple point T. The slip line is created by the sharp transverse

motion of the transverse wave and the triple point. As the triple point gets closer to the lower wall surface, the bow shock intensity increases, resulting in a faster motion, which also leads to significantly rolled suction vortices on the shear layer of the slip line as shown in Figure 4b. These vortex structures formed by the KHI promote turbulent mixing of combustion products with unburned material, further contributing to the consumption of unburned jets.

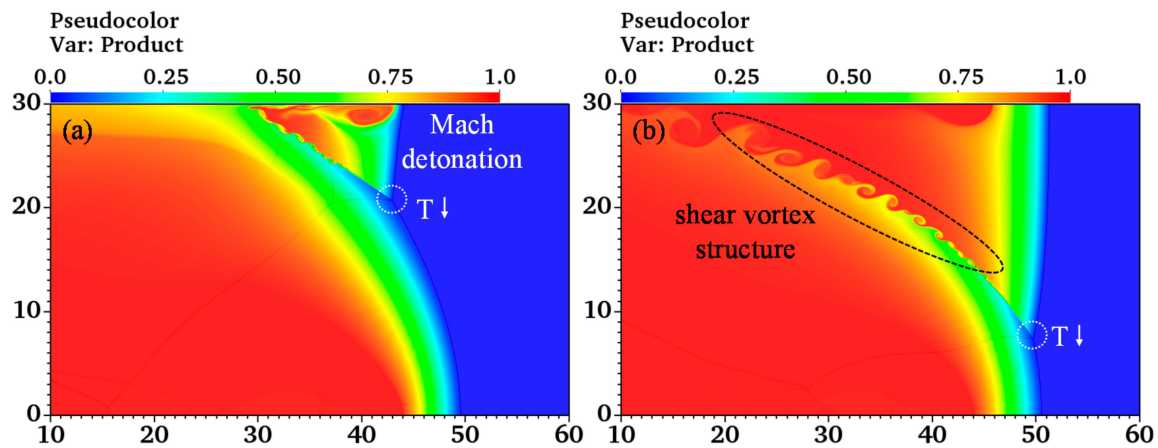


Figure 4. Contour of reaction progress variable after single-jet initiation: (a) $t = 195 \mu\text{s}$; (b) $t = 220 \mu\text{s}$.

Figure 5 demonstrates the propagation of the detonation under the single-jet initiation method. The local detonation expands to the lower wall surface as the triple point moves downward, as shown in Figure 5a. When the triple point collides with the lower wall surface, detonation combustion of the whole channel is achieved. In Figure 5a,b, the pressures after the transverse wave are 240.5 and 287.2 kPa, respectively, indicating that after the collision with the wall, the transverse wave intensity increases. Moreover, the triple points are reversed and propagate up. After the transverse wave sweeps through the shear layer of the hot jet, the pressure wave is generated, and the detonation propagates forward as a single-headed mode. The shear layer formed under the continuous injection of hot jets is also equivalent to an aerodynamic ramp that continues to drive the forward propagation of the detonation wave.

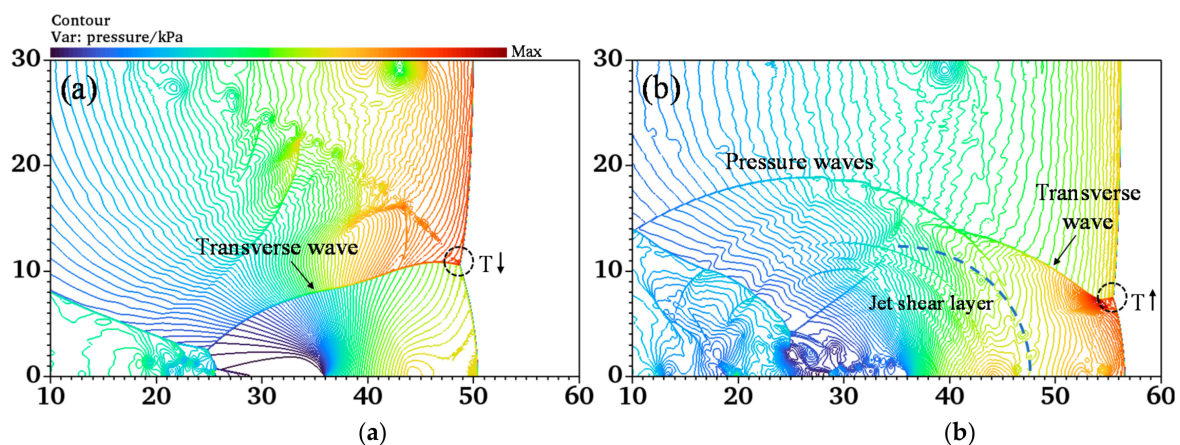


Figure 5. Pressure isolines showing the propagation of triple points in detonation initiation of a single-jet: (a) $t = 215 \mu\text{s}$; (b) $t = 240 \mu\text{s}$.

3.2. Analysis of the Detonation Induced by Symmetric-Jet

As shown in Figure 6a, the hot jets from the upper and lower walls are injected into the flow field to induce two bow shock waves. The structure of the bow shocks is symmetrical

because the parameters of the two hot jets are set identically. Under the current conditions, the strength of the hot jets is not sufficient to achieve instantaneous detonation. After the gas mixture is compressed by the bow shock, the pressure rises, and thus a combustion zone is created behind the bow shock. The continuous injection of the hot jet further develops the bow shock and gradually extends to the opposite side. As shown in Figure 6b, the two bow shocks interact with each other in the center of the channel to form a regular reflection, and a high-pressure region is formed at the interaction. With the enhancement of the reflected shock wave, the regular reflection is transformed into two double Mach reflections. As shown in Figure 6c, the reflection point develops into a Mach stem. The structure of the shock front from top to bottom is bow shock-Mach stem-bow shock. At this time, Mach reflections on the wall caused by the reflected shock can also be observed. The propagation of the triple points raises the Mach stem height and develops further from the center of the channel to both sidewalls. As shown in Figure 6d, two symmetrical triple points T_1 and T_2 are observed at the shock front, and the red arrows indicate the direction of motion of the triple points.

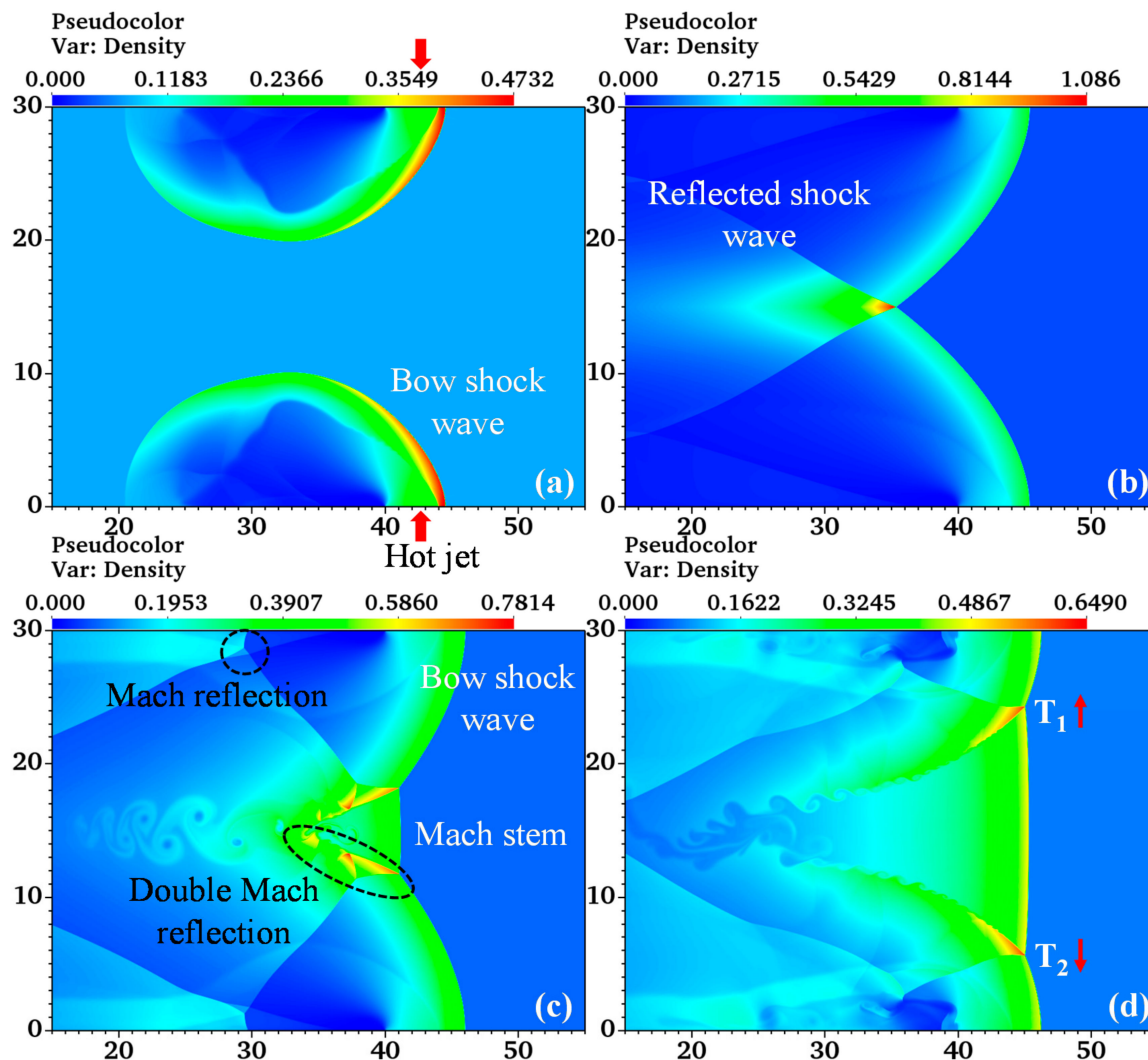


Figure 6. Density contours showing detonation initiation in straight channel, with continuous injection of a symmetric jet: (a) $t = 110 \mu\text{s}$; (b) $t = 130 \mu\text{s}$; (c) $t = 160 \mu\text{s}$; (d) $t = 180 \mu\text{s}$.

Analysis of the detonation initiation process of single- and symmetric-jet can be seen. In the single-jet initiation method, the bow shock is reflected on the upper wall and generates a Mach stem, resulting in the emergence of a local detonation and gradually

initiating the whole flow. By contrast, in the symmetric-jet initiation method, the appearance of the Mach stem is due to the interaction of the upper and lower bow shock, and the emergence of the position is on the central axis of the channel. To analyze the combustion after the shock surface under the symmetric-jet conditions, Figure 7 shows the emergence of the Mach stem and its development toward the walls on both sides. As shown in Figure 7a, the Mach stem between the triple points T_1 and T_2 is tightly coupled to the combustion surface, indicating that a Mach detonation has formed. However, the weaker strength of the bow shock on both sides of the triple point T_1 and T_2 makes the formation of two unburned jets between the Mach stem and the bow shocks. In addition, the bow shock in the middle of the channel has the lowest intensity and the weakest effect on the compression of the mixture. Therefore, even after the appearance of the Mach stem, there is still a large amount of incompletely reacted gas behind the interaction of the upper and lower bow shocks. Moreover, multiple mushroom vortex structures formed by the RMI are also observed in this region. These vortex structures are developed from the rear of the slip lines. Comparing Figure 7a,b, it is found that these vortex structures generated by RMI enhance the turbulent mixing of combustion products and reactants to promote turbulent combustion in the middle of the flow. In addition, the small-scale KHI vortices along the slip line also greatly enhance the mixing efficiency of reactants and combustibles and promotes the consumption of unburned jets. This process gradually makes the combustion reaction after the detonation complete, while the release of a large amount of chemical energy can also effectively promote the development and propagation of the detonation wave.

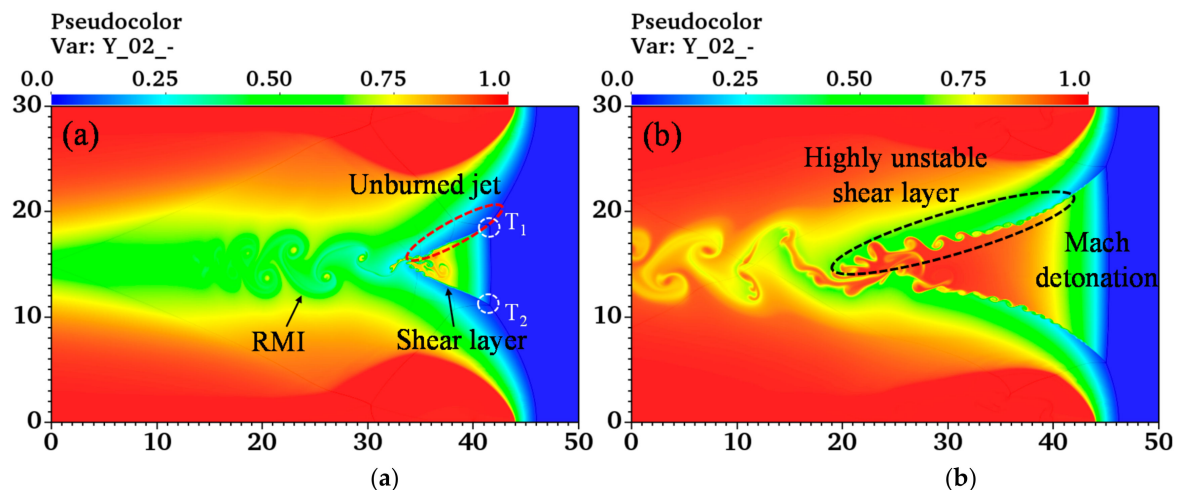


Figure 7. Contour of reaction progress variable after symmetric-jet initiation: (a) $t = 162.5 \mu s$; (b) $t = 180 \mu s$.

To further explore the large-scale RMI vortices behind the slip line, Figure 8 illustrates the generation and consumption mechanism of this mushroom vortex structure. The inconsistency in the directions of the density and pressure gradient produces a large baroclinic torque ($\nabla \rho \times \nabla p$), causing the RMI at the interface of the unburned jet [43]. The left side of Figure 8 shows the contours of the baroclinic torque. Comparing Figure 8a,b, after the Mach stem in the middle of the channel appears, the gas mixture reacts quickly through its adiabatic compression, which also causes the combustible gas and products of high-speed reaction to be squeezed, forming a backward jet and a forward jet. The contours of the baroclinic torque show that there is a strong baroclinic torque at the backward jet. This also leads to a faster growth rate of the backward jet, as shown in the contour of the product on the right. The “cap” structure in the RMI vortex is defined as C_i , and i is used to classify the number of observed vortices. The stronger baroclinic torque leads to the continuous creation of new vortices. The increasing number and size of the RMI vortices enlarge the contact surface between unburned and burned materials, intensifying the chemical reaction. Comparing Figure 8c,d, it can be seen that the baroclinic torque near the forward and

backward jets disappears with the propagation of the triple point. The right-hand product cloud also further shows that during this period, new mushroom vortices are no longer generated, while turbulent mixing effects lead to the gradual depletion of the previous RMI vortices. The gas mixture in the middle of the flow field gradually reacts completely.

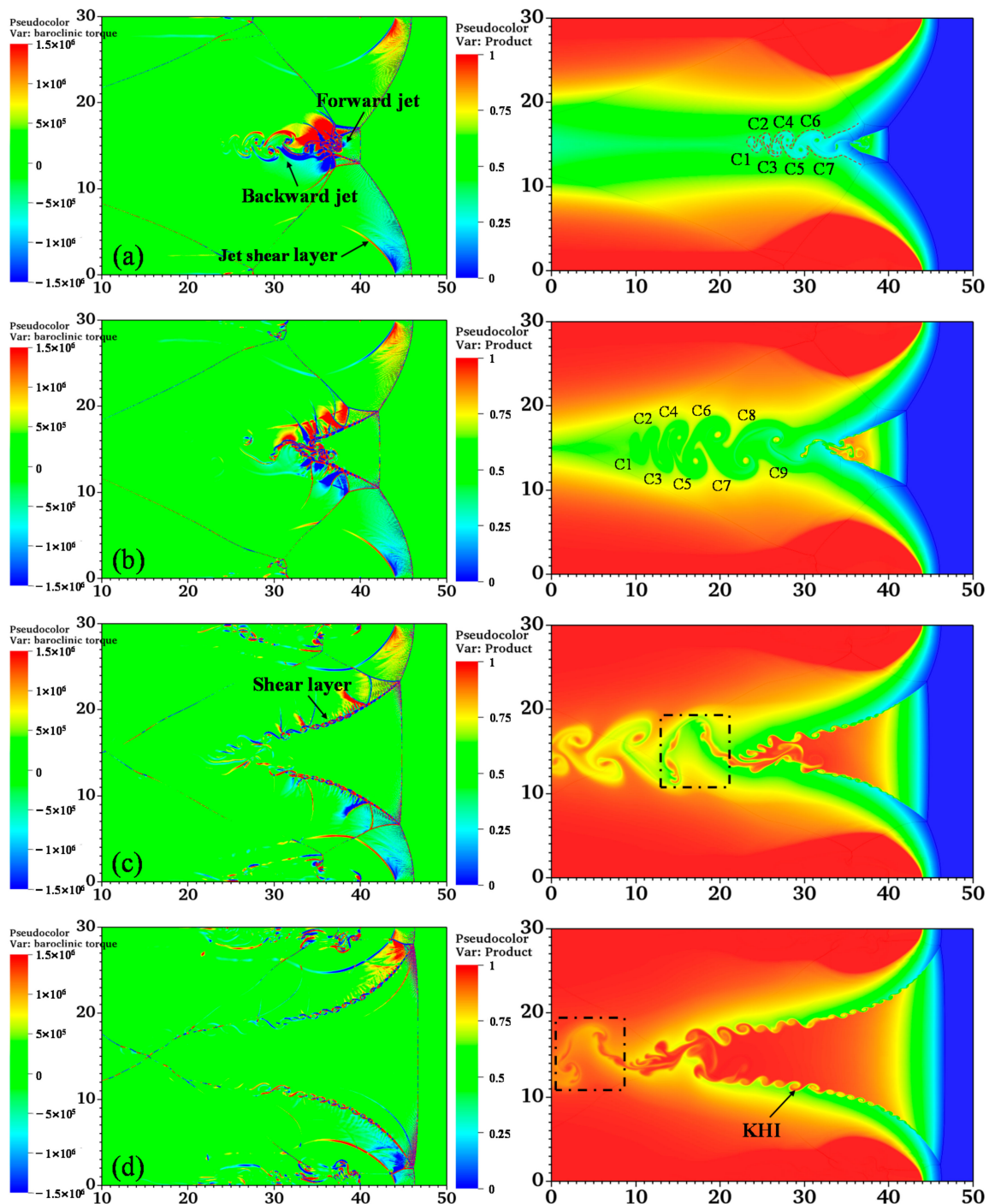


Figure 8. Large-scale RMI vortices in detonation structure after local detonation generation: (a) $t = 155 \mu\text{s}$; (b) $t = 165 \mu\text{s}$; (c) $t = 177.5 \mu\text{s}$; (d) $t = 187.5 \mu\text{s}$. Left column shows contour of baroclinic torque, $\nabla\rho \times \nabla p$. Right column shows contour of corresponding reaction progress variable.

Figure 9 shows the propagation of the triple points after the local detonation is generated using the symmetric-jet initiation method. It also indicates the detonation initiation process of the whole flow and the propagation of the detonation wave in the channel.

The black arrow identifies the direction of propagation of the triple point. As shown in Figure 9a, after the local detonation is formed, the triple points T_1 and T_2 propagate up and down the wall, respectively. At the same time, the Mach stem height is raised, and the local detonation is expanded. When the triple points T_1 and T_2 collide with the wall and then move in the opposite direction, the initiation of the entire flow field is achieved, as shown in Figure 9b. In Figure 9c, the two triple point collision leads to an increase in local pressure and temperature, and a rapid increase in the rate of the chemical reaction. The triple points again reverse their motion and approach the walls on both sides, as shown in Figure 9d. In the symmetric-jet initiation method, two triple points with opposite propagation are formed on the detonation front, and the detonation shows a double-headed self-sustaining propagation. In addition, under the continuous injection of hot jets, the shear layer formed by hot jets at the upper and lower walls constitutes a compression channel, which raises the pressure behind the detonation wave and promotes the forward propagation of the detonation wave.

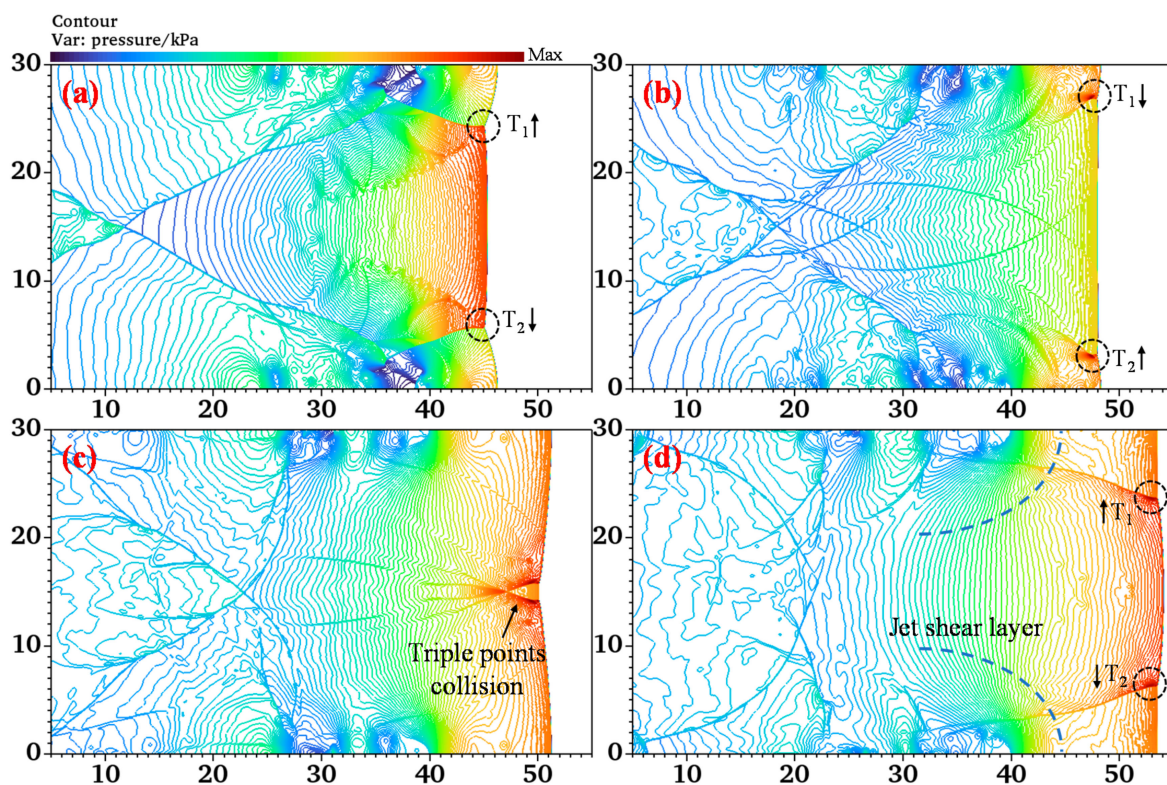


Figure 9. Pressure isolines showing propagation of triple points in detonation initiation of a symmetric-jet: (a) $t = 180 \mu\text{s}$; (b) $t = 195 \mu\text{s}$; (c) $t = 207.5 \mu\text{s}$; (d) $t = 220 \mu\text{s}$.

From the above analysis, it is clear that there are differences in the detonation initiation process under the two different initiation methods, which also lead to significant differences in the location of the local detonation and the characteristics of the detonation front. Figure 10a shows the trajectory of the detonation front based on the two jet initiation methods. The trajectory can be classified into two stages. In the first stage, the hot jet is injected into the flow field and induced to form a bow shock. At this time, the trajectory captures the position of the bow shock, and the line segment is relatively smooth. The second stage is the detonation front after the flow field is initiated. When the hot jet is continuously injected, the trajectories of wave surface under the two initiation methods are straight lines, and the slopes are almost the same. This indicates that regardless of whether the single- or symmetric-jet is used at this stage, under the same intensity of the hot jet, the propagation velocity of the formed detonation wave is almost equal. Based on the slope of the curve, the average forward velocity Δv of the detonation wave is approximately

266 m/s, and the corresponding overdrive degree f is 1.363 ($f = \left(\frac{V_{CJ} + \Delta v}{V_{CJ}}\right)^2$). When the double-jet is shutdown at 200 μ s, the detonation wave surface exhibits regular periodic oscillations, whose period is approximately 40 μ s. At this time, the average relative propagation velocity of the detonation wave is $\Delta v = 57.9$ m/s, the forward velocity is decreased by approximately 70%, and the corresponding overdrive degree f is decreased to 1.073. It can be assumed that the overdrive detonation wave gradually decays into periodic-oscillation CJ detonation.

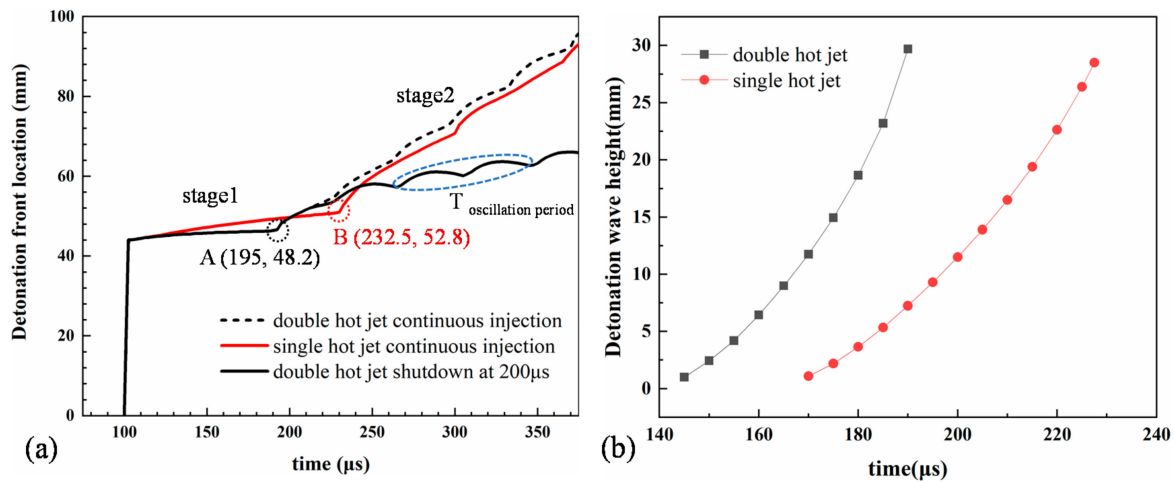


Figure 10. (a) Trajectory of detonation front along lower wall. (b) Detonation wave height.

Comparing the abscissas of points A and B as shown in Figure 10a, it is discovered that using the single-jet requires a longer time to complete initiation. However, in the symmetric-jet initiation mode, the two triple points propagate toward the wall at the same time, which can shorten the time of initiation. This also leads to a more rapid increase in the height of the local detonation wave (Mach stem) under a double-jet injection, as shown in Figure 10b. Furthermore, by comparing the coordinates (the ordinate values of points A and B) at the moments when the initiation is achieved under the two methods, it is clear that the initiation achieved within a certain distance by the symmetric-jet is approximately 4.6 mm shorter than that for single-jet. This is useful for practical applications.

Through a detailed analysis of the above two initiation methods, it is found that the change in the flow area after the detonation wave caused by changing the initiation method of the jet has little effect on the propagation speed of the detonation. However, regardless of the mode of initiation, the intensity of the jet-induced bow shock is critical to initiation. For the symmetric-jet initiation mechanism, the low intensity of bow shock may lead to insufficient energy generated by collision reflection of shock to form Mach reflection, thus affecting the detonation initiation process. Therefore, it is necessary to further induce the effect of the intensity of the bow shock on the symmetric-jet initiation.

3.3. Effects of Diameter of Hot Jet D_j on Detonation Initiation

In the previous section, it was shown that the intensity of the jet-induced bow shock depends mainly on the diameter of the hot jet D_j , pipe height H_p , and the momentum flux ratio J , expressed as follows:

$$J = \gamma_j P_j Ma_j^2 / \gamma_\infty P_\infty Ma_\infty^2 \tag{5}$$

This section explores the effect of jet diameter D_j on the double jet detonation initiation process.

Based on a basic calculation example ($D_j = 4.0$ mm), four other jet diameters are considered (while other parameters are maintained), leading to five in total as follows: $D_{j1} = 2.5$ mm, $D_{j2} = 3.0$ mm, $D_{j3} = 3.5$ mm, $D_{j4} = 4.0$ mm, and $D_{j5} = 4.5$ mm.

The penetration height of jet formula is expressed as follows [44,45]:

$$H_p = 2.713D_j^{0.719}J^{0.273} \tag{6}$$

When the jet diameter increases from 2.5 mm to 4.5 mm, the momentum flux ratio J remains unchanged, whereas the jet penetration increases from 4.5028 to 6.8710. This means the strength of the bow shock increases accordingly. Table 4 lists the penetration height H_p and the momentum flux ratio J of the dual-jet for different diameters. Figure 11 shows the ignition time t_1 and the time t_2 of the initiation completed for five different jet diameters, with a time step of 2.5 μs .

Table 4. Momentum flux ratio J and penetration height H_p under different jet diameters.

D_j (mm)	2.5	3	3.5	4	4.5
J	0.5727	0.5727	0.5727	0.5727	0.5727
H_p (mm)	4.5028	5.1335	5.7352	6.3131	6.8710

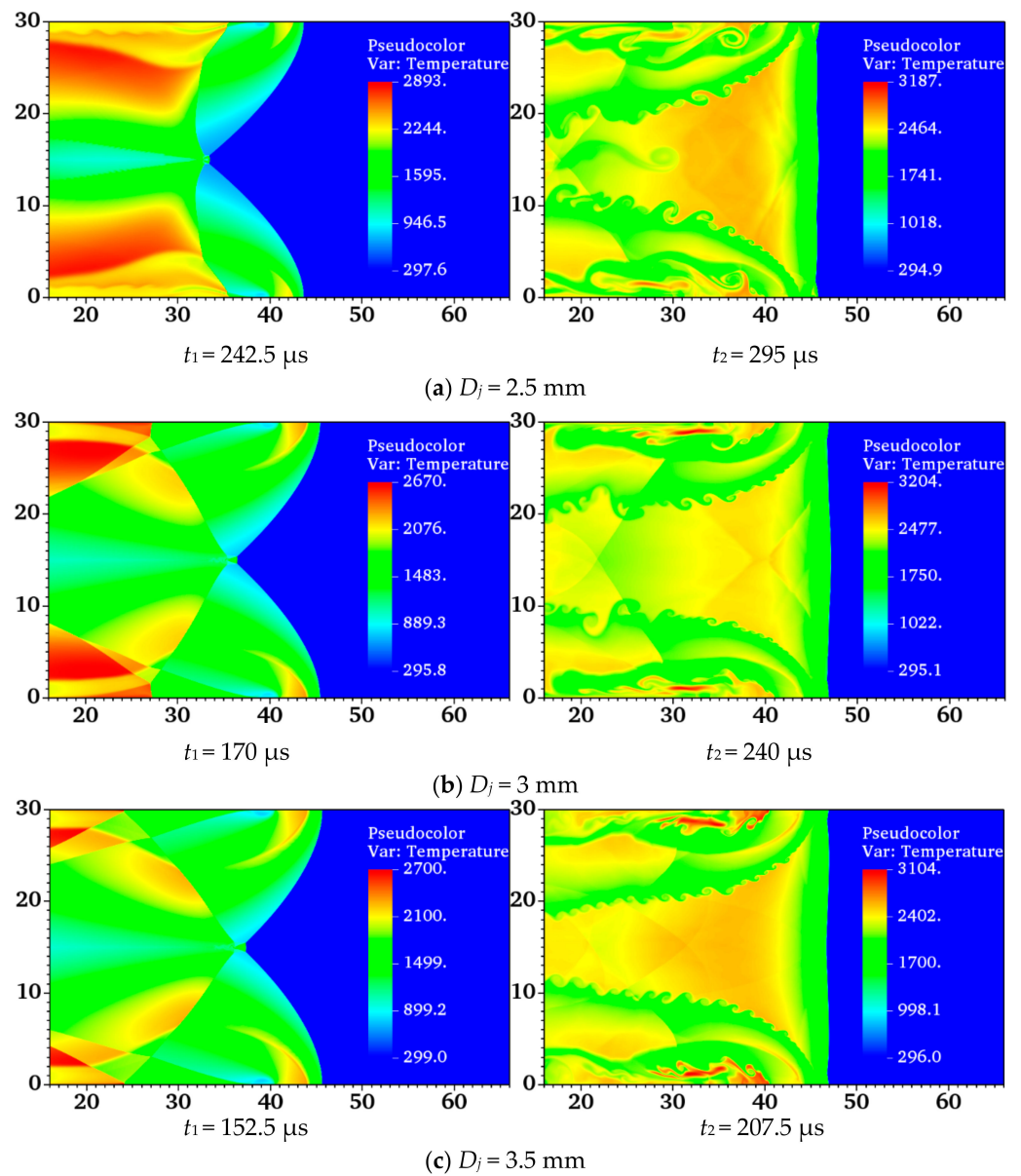


Figure 11. Cont.

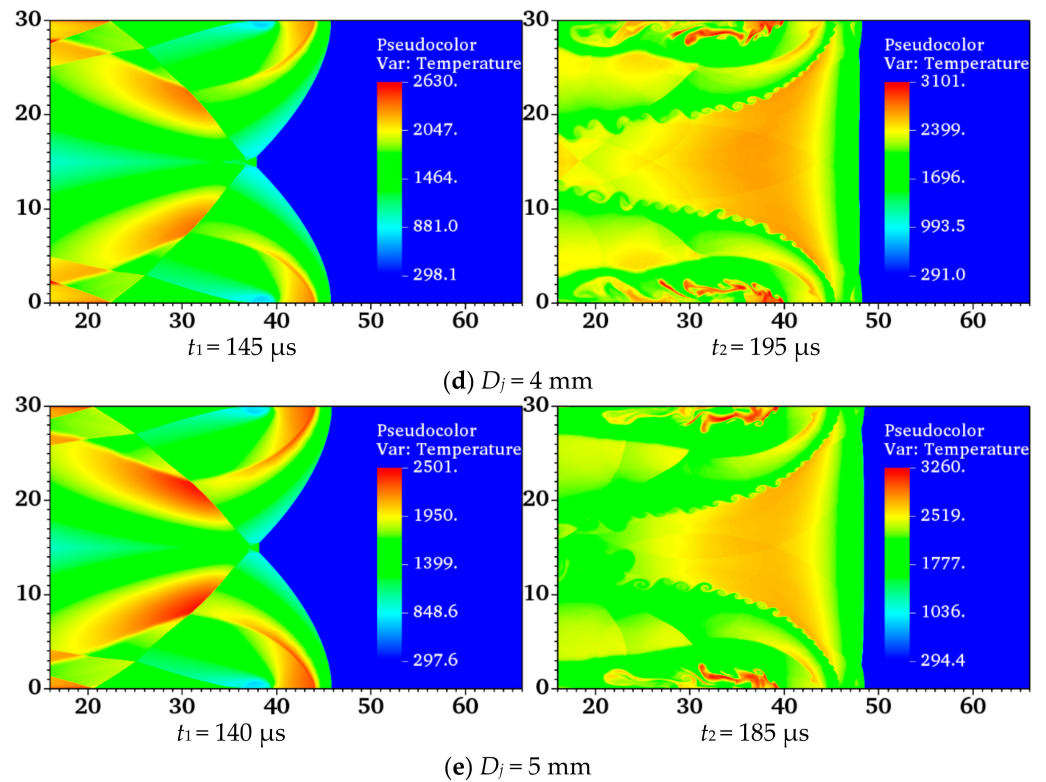


Figure 11. Contours of temperature for successful detonation initiation.

Table 5 lists the location of the ignition point (Mach stem) and the times t_1 and t_2 during the process of detonation initiation under five numerical simulation conditions. It can be seen in the table that the stronger jet penetration under the larger diameter of jet results in stronger and steeper induced bow shocks. As a result, the intersection point of the two bow shocks is more forward, which also leads to a more forward location for the initiation point to appear. In addition, as the jet diameter increases, the detonation initiation becomes more rapid.

Table 5. Abscissa of the Mach stems and critical moments t_1 and t_2 in initiation under different jet diameters.

D_j (mm)	2.5	3	3.5	4	4.5
x (mm)	33.47	36.20	37.15	37.86	38.06
t_1 (μ s)	242.5	170	152.5	145	140
t_2 (μ s)	295	240	207.5	195	185

Observing the right hand part of Figure 11, in the case of the jet diameter of 3–4.5 mm, the secondary reflected shock wave formed at the two wall sides by the reflected shock behind the Mach stem is observed. However, at a jet diameter of 2.5 mm, this reflected shock is not observed. To analyze the cause of this phenomenon, Figure 12 shows the shock wave interaction process before initiation at a jet diameter of 2.5 mm. As shown in Figure 12a, the interaction between the bow shocks produces reflected shock waves, and as the intensity of the reflected shocks increases, the Mach reflections are formed at the wall. Thereafter, the Mach reflections move toward the intersection of the bow shocks. As shown in Figure 12b, the two Mach reflections interact with each other to form multiple shocks and expansion waves between the upper and lower slip lines. When the triple points of the two Mach reflections collide with each other, the large amount of energy generated drives the formation of the Mach stem in the middle of the flow field to achieve initiation.

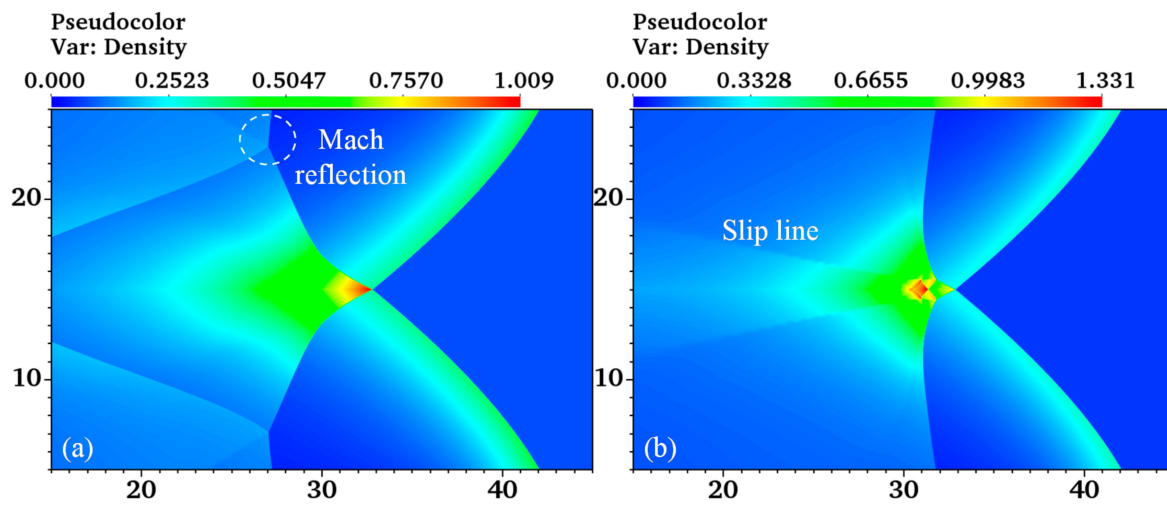


Figure 12. Shock wave interaction process in a jet diameter of 2.5 mm: (a) $t = 200 \mu\text{s}$; (b) $t = 235 \mu\text{s}$.

As shown in Figure 13, after the initiation is completed, the detonation waves under different cases are overdriven forward at a stable speed. As shown in Table 6, when the jet diameter increased, the relative propagation velocity Δv , absolute propagation velocity V , and overdrive degree f of the detonation wave also increased. This is because as the jet diameter increased, the jet penetration expanded and the height of the shear layer formed by the hot jets rose, which further compressed the gas mixture after the detonation wave, thereby accelerating the propagation of the detonation wave.

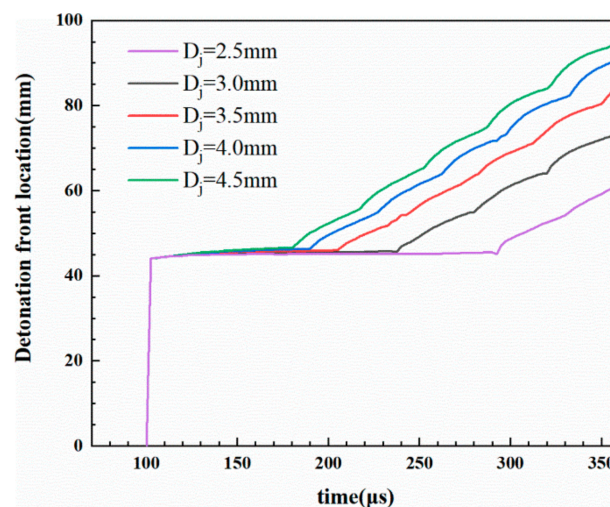


Figure 13. Trajectory of detonation front along lower wall based on five jet diameters.

Table 6. Detonation wave parameters for different jet diameters.

D_j (mm)	Δv (m/s)	V (m/s)	f
2.5	213.75	1801.59	1.287
3.0	237.87	1820.19	1.322
3.5	249.74	1836.64	1.339
4.0	266.02	1853.48	1.363
4.5	279.05	1866.50	1.382

Figure 14 shows the critical moment of initiation for single-jet and symmetric-jet for different jet diameters. As can be seen from the figure, in the interval of 3.0–4.5 mm jet diameter, comparing the time t_1 between symmetric- and single-jet, it can be seen that

the local detonation appears earlier and the velocity of initiation is more rapid with the symmetric-jet. Comparing time t_2 when the jet diameter of 3.0–4.5 mm, the symmetrical-jet can be seen to shorten the time of the first collision between the triple point and the wall, and speed up the completion of the initiation. When the jet diameter is 2.5 mm, the bow shock induced by two jets is not strong enough. The interaction of bow shocks cannot directly form a local detonation, but this can be initiated by the collision of two Mach reflections behind the intersection.

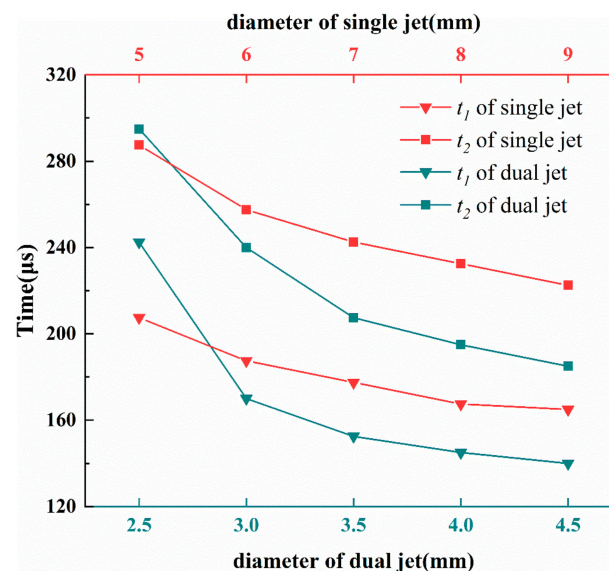


Figure 14. Two critical initiation times for different jet diameters based on two initiation methods. The upper and lower horizontal coordinates correspond to the same total jet intensity.

4. Conclusions

In this study, the two-dimensional Navier–Stokes equation is solved using the adaptive mesh refinement code AMROC, which is used to perform a high-resolution numerical simulation of the supersonic gaseous detonation initiated by a symmetric-jet. The following conclusions are drawn:

- (1) The symmetric hot jets significantly change the process of detonation initiation. The jet-induced bow shocks interact with each other forming a local detonation. This new flow field structure also makes the interaction of the shear layer behind the triple points form a periodic shedding vortex structure, which enhances the diffusion effect in the unburned region.
- (2) Compared to a single-jet, using a symmetric-jet (with a diameter of 4 mm) can significantly reduce the distance to complete initiation (by about 52%). The symmetric-jet initiation method helps to reduce the length of the combustion chamber and facilitates the lightweight design of the engine.
- (3) In the action of the propagation of the triple points, the development process of detonation combustion is more rapid when using a symmetric-jet. In addition, the detonation wave formation by a single-jet exhibits single-headed self-sustaining propagation, while the symmetric-jet condition exhibits double-headed self-sustaining propagation. However, neither operating condition has significant effect on the degree of detonation overdrive.
- (4) The jet strength has a significant effect on the process of symmetric-jet initiation. In this study, when the jet diameter decreases to 2.5 mm, the local detonation relies on the two Mach reflections formed on the wall to produce a second collision at the intersection. Thus, the wall boundary condition of the engine combustion chamber needs to be considered at this time. This also leads to a longer time to complete initiation relative to the single-jet approach.

Author Contributions: Conceptualization, J.D. and L.P.; methodology, J.D. and L.P.; Investigation, L.P.; writing—original draft preparation, L.P.; writing—review and editing, J.D. and L.P. All authors have read and agreed to the published version of the manuscript.

Funding: This research received no external funding.

Conflicts of Interest: The authors declare no conflict of interest.

References

1. Kireeti, S.K.; Ravikiran Sastry, G.; Gugulothu, S.K.; Deepanraj, B.; Loke Show, P.; Xia, A.; Arthi, M. Numerical investigations on the implication of hydrogen fuel jet injection pressure on the performance characteristics in a multi-strut in a double-dual cavity-based scramjet combustor. *Fuel* **2022**, *324*, 124528. [[CrossRef](#)]
2. Sharma, V.; Eswaran, V.; Chakraborty, D. Determination of optimal spacing between transverse jets in a scramjet engine. *Aerosp. Sci. Technol.* **2020**, *96*, 105520. [[CrossRef](#)]
3. Wolański, P. Detonative propulsion. *Proc. Combust. Inst.* **2013**, *34*, 125–158. [[CrossRef](#)]
4. Tunik, Y.V.; Mayorov, V.O. Busemann diffuser for supersonic ramjet engine with detonation combustion of hydrogen-air mixture. *Int. J. Hydrogen Energ.* **2022**, *47*, 21828–21840. [[CrossRef](#)]
5. Phylippov, Y.G.; Dushin, V.R.; Nikitin, V.F.; Nerchenko, V.A.; Korolkova, N.V.; Guendugov, V.M. Fluid mechanics of pulse detonation thrusters. *Acta Astronaut.* **2012**, *76*, 115–126. [[CrossRef](#)]
6. Wang, G.; Liu, S.; Peng, H.; Liu, W. Experimental Investigation of a Cylindrical Air-Breathing Continuous Rotating Detonation Engine with Different Nozzle Throat Diameters. *Aerospace* **2022**, *9*, 267. [[CrossRef](#)]
7. Yan, C.; Teng, H.H.; Mi, X.C.; Ng, H.D. The Effect of Chemical Reactivity on the Formation of Gaseous Oblique Detonation Waves. *Aerospace* **2019**, *6*, 62. [[CrossRef](#)]
8. Li, C.; Kailasanath, K. Detonation initiation by Annular-Jet-Induced imploding shocks. *J. Propul. Power* **2005**, *21*, 183–186. [[CrossRef](#)]
9. Liang, J.; Cai, X.; Lin, Z.; Deiterding, R. Effects of a hot jet on detonation initiation and propagation in supersonic combustible mixtures. *Acta Astronaut.* **2014**, *105*, 265–277. [[CrossRef](#)]
10. Gordon, P.V.; Kagan, L.; Sivashinsky, G. Parametric transition from deflagration to detonation revisited: Planar geometry. *Combust. Flame* **2020**, *211*, 465–476. [[CrossRef](#)]
11. Knystautas, R.; Lee, J.H.; Moen, I.; Wagner, H.G. Direct Initiation of Spherical Detonation by a Hot Turbulent Gas Jet. *Symp. (Int.) Combust.* **1979**, *17*, 1235–1245. [[CrossRef](#)]
12. Ishii, K.; Kataoka, H.; Kojima, T. Initiation and propagation of detonation waves in combustible high speed flows. *Proc. Combust. Inst.* **2009**, *32*, 2323–2330. [[CrossRef](#)]
13. Han, X.; Zhou, J.; Lin, Z. Experimental investigations of detonation initiation by hot jets in supersonic premixed flows. *Chin. Phys. B* **2012**, *21*, 309–313. [[CrossRef](#)]
14. Chen, W.; Liang, J.; Cai, X.; Lin, Z. The initiation and propagation of detonation in supersonic combustible flow with boundary layer. *Int. J. Hydrogen Energ.* **2018**, *43*, 12460–12472. [[CrossRef](#)]
15. Cirak, F.; Deiterding, R.; Mauch, S.P. Large-scale fluid-structure interaction simulation of viscoplastic and fracturing thin-shells subjected to shocks and detonations. *Comput. Struct.* **2007**, *85*, 1049–1065. [[CrossRef](#)]
16. Deiterding, R. A parallel adaptive method for simulating shock-induced combustion with detailed chemical kinetics in complex domains. *Comput. Struct.* **2009**, *87*, 769–783. [[CrossRef](#)]
17. Cai, X.; Liang, J.; Deiterding, R.; Lin, Z. Numerical Investigation on Detonation Control Using a Pulse Hot Jet in Supersonic Combustible Mixture. *Combust. Sci. Technol.* **2016**, *188*, 1674–1690. [[CrossRef](#)]
18. Peng, H.; Huang, Y.; Deiterding, R.; Luan, Z.; Xing, F.; You, Y. Effects of jet in crossflow on flame acceleration and deflagration to detonation transition in methane–oxygen mixture. *Combust. Flame* **2018**, *198*, 69–80. [[CrossRef](#)]
19. Peng, H.; Huang, Y.; Deiterding, R.; You, Y.; Luan, Z. Effects of Transverse Jet Parameters on Flame Propagation and Detonation Transition in Hydrogen-Oxygen-Argon Mixture. *Combust. Sci. Technol.* **2021**, *193*, 1516–1537. [[CrossRef](#)]
20. Bulat, M.P.; Bulat, P.V.; Denissenko, P.V.; Esakov, I.I.; Grachev, L.P.; Volkov, K.N.; Volobuev, I.A. Ignition of lean and stoichiometric air–propane mixture with a subcritical microwave streamer discharge. *Acta Astronaut.* **2017**, *150*, 153–161. [[CrossRef](#)]
21. Wang, Z.; Pan, Z.; Huang, J.; Wei, L.; Wang, Y.; Wang, Y. Effects of double-jet positions on detonation initiation characteristics. *Aerosp. Sci. Technol.* **2020**, *97*, 105609. [[CrossRef](#)]
22. Mazaheri, K.; Mahmoudi, Y.; Sabzpooshani, M.; Radulescu, M.I. Experimental and numerical investigation of propagation mechanism of gaseous detonations in channels with porous walls. *Combust. Flame* **2015**, *162*, 2638–2659. [[CrossRef](#)]
23. Mahmoudi, Y.; Mazaheri, K. High resolution numerical simulation of triple point collision and origin of unburned gas pockets in turbulent detonations. *Acta Astronaut.* **2015**, *115*, 40–51. [[CrossRef](#)]
24. Miao, S.; Zhou, J.; Liu, S.; Cai, X. Formation mechanisms and characteristics of transition patterns in oblique detonations. *Acta Astronaut.* **2018**, *142*, 121–129. [[CrossRef](#)]
25. Yuan, X.; Zhou, J.; Liu, S.; Lin, Z. Diffraction of cellular detonation wave over a cylindrical convex wall. *Acta Astronaut.* **2019**, *169*, 94–107. [[CrossRef](#)]
26. Strehlow, R.A. Gas phase detonations: Recent developments. *Combust. Flame* **1968**, *12*, 81–101. [[CrossRef](#)]

27. Pintgen, F.; Eckett, C.A.; Austin, J.M.; Shepherd, J.E. Direct observations of reaction zone structure in propagating detonations. *Combust. Flame* **2003**, *133*, 211–229. [[CrossRef](#)]
28. Gorbatenko, I.; Bradley, D.; Tomlin, A.S. Auto-ignition and detonation of n-butanol and toluene reference fuel blends (TRF). *Combust. Flame* **2021**, *229*, 111378. [[CrossRef](#)]
29. Dai, J.; Xu, F.; Cai, X.; Mahmoudi, Y. Effects of velocity shear layer on detonation propagation in a supersonic expanding combustor. *Phys. Fluids* **2021**, *33*, 105110. [[CrossRef](#)]
30. Bakalis, G.; Tang-Yuk, K.C.; Mi, X.; Nikiforakis, N.; Ng, H.D. Numerical simulation of deflagration-to-detonation transition via shock–multiple flame kernels interactions. *Comput. Math. Appl.* **2020**, *83*, 111–126. [[CrossRef](#)]
31. Ziegler, J.L.; Deiterding, R.; Shepherd, J.E.; Pullin, D.I. An adaptive high-order hybrid scheme for compressive, viscous flows with detailed chemistry. *J. Comput. Phys.* **2011**, *230*, 7598–7630. [[CrossRef](#)]
32. Chen, W.; Liang, J.; Cai, X.; Mahmoudi, Y. Three-dimensional Simulations of Detonation Propagation in Circular Tubes: Effects of Jet Initiation and Wall Reflection. *Phys. Fluids* **2020**, *32*, 046104.
33. Varatharajan, B.; Williams, F.A. Chemical-kinetic descriptions of high-temperature ignition and detonation of acetylene-oxygen-diluent systems. *Combust. Flame* **2001**, *124*, 624–645. [[CrossRef](#)]
34. Liu, X.; Chen, Y.; Xia, Z.; Wang, J. Numerical study of the reverse-rotating waves in rotating detonation engine with a hollow combustor. *Acta Astronaut.* **2020**, *170*, 421–430. [[CrossRef](#)]
35. Ng, H.D. Effects of activation energy on the instability of oblique detonation surfaces with a one-step chemistry model. *Phys. Fluids* **2018**, *30*, 106110. [[CrossRef](#)]
36. Sharpe, G.J.; Radulescu, M.I. Statistical analysis of cellular detonation dynamics from numerical simulations: One-step chemistry. *Combust. Theor. Model.* **2011**, *15*, 691–723. [[CrossRef](#)]
37. Lappa, M. A mathematical and numerical framework for the analysis of compressible thermal convection in gases at very high temperatures. *J. Comput. Phys.* **2016**, *313*, 687–712. [[CrossRef](#)]
38. Zhang, Y.; Deng, W.; Zhu, J. A new sixth-order finite difference WENO scheme for fractional differential equations. *J. Sci. Comput.* **2021**, *87*, 73. [[CrossRef](#)]
39. Ketcheson, D.I. Highly efficient strong stability preserving Runge-Kutta methods with Low-Storage Implementations. *SIAM J. Sci. Comput.* **2008**, *30*, 2113–2136. [[CrossRef](#)]
40. Kaps, P.; Rentrop, P. Generalized Runge-Kutta methods of order four with stepsize control for stiff ordinary differential equations. *Numer. Math.* **1979**, *33*, 55–68. [[CrossRef](#)]
41. Deiterding, R.; Bader, G. *High-Resolution Simulation of Detonations with Detailed Chemistry*; Springer: Berlin/Heidelberg, Germany, 2005; pp. 69–91.
42. Cai, X.; Liang, J.; Lin, Z.; Deiterding, R.; Liu, Y. Parametric study of detonation initiation using a hot jet in supersonic combustible mixtures. *Aerosp. Sci. Technol.* **2014**, *39*, 442–455. [[CrossRef](#)]
43. Peng, N.; Yang, Y.; Wu, J.; Xiao, Z. Mechanism and modelling of the secondary baroclinic vorticity in the Richtmyer–Meshkov instability. *J. Fluid Mech.* **2021**, *911*, A56. [[CrossRef](#)]
44. Rothstein, A.; Wantuck, P. A study of the normal injection of hydrogen into a heated supersonic flow using planar laser-induced fluorescence. In Proceedings of the 28th Joint Propulsion Conference and Exhibit, Nashville, TN, USA, 6–8 July 1992.
45. Ben-Yakar, A.; Mungal, M.G.; Hanson, R.K. Time evolution and mixing characteristics of hydrogen and ethylene transverse jets in supersonic crossflows. *Phys. Fluids* **2006**, *18*, 26101. [[CrossRef](#)]